**Proceedings of IDETC/CIE 2006:**
**32nd Design Automation Conference**
**September 10-13, 2006, Philadelphia, Pennsylvania**

# DETC2006-99329

# MATERIAL PROPERTY IDENTIFICATION AND SENSITIVITY ANALYSIS USING INDENTATION AND FEM

**Long Ge**
Mechanical & Aerospace Engineering
University of Florida, PO Box 116250
Gainesville, FL 32611
ccdell@ufl.edu

**Nam Ho Kim**
Mechanical & Aerospace Engineering
University of Florida, PO Box 116250
Gainesville, FL 32611
nkim@ufl.edu

**Gerald R. Bourne**
Material Science & Engineering
University of Florida, PO Box 116400
Gainesville, FL 32611
grb@ufl.edu

**W. Gregory Sawyer**
Mechanical & Aerospace Engineering
University of Florida, PO Box 116300
Gainesville, FL 32611
wgsawyer@ufl.edu

## Abstract

Mechanical properties of materials in small-scale applications, such as thin coatings, are often different from those of bulk materials due to the difference in the manufacturing process. Indentation has been a convenient tool to study the mechanical properties in such applications. In this paper, a numerical technique is proposed that can identify the mechanical properties by minimizing the difference between the results from indentation experiments and those from finite element analysis. First, two response surfaces are constructed for loading and unloading curves from the indentation experiment of a gold film on the silicon substrate. Unessential coefficients of the response surface are then removed based on the test statistics. Different from the traditional methods of identification, the tip geometry of the indenter is included because its uncertainty significantly affects the results. In order to validate the accuracy and stability of the method, the sensitivity of the identified material properties with respect to each coefficient is analyzed.

## 1. Introduction

Micro-scale materials show different properties from those of bulk materials.[1] Recent advances in technology allow experiments to be carried out on such a small scale. Indentation is a powerful tool to study mechanical properties. It is widely used in the automotive, semiconductor, biomedical, and magnetic recording industry, and by academics.[2-4] In this paper, a numerical method is presented that can identify the material properties using the data obtained from indentation experiments.

Recently, numerical studies emerged to catch up with the experimental research on micro-scales. Numerical methods can determine properties or parameters that are difficult to obtain from experiments. They are able to elucidate physical mechanisms or procedures that are difficult in experiments. They can also provide suggestions and give a guide for experiments.

For nano-scales molecular dynamics (MD) simulation, pioneered by Landman et al.[5], is a useful tool for analyzing nanometric or atomic phenomena, including indentation and scratch. Using MD simulation, indentation and scratch of different materials have been broadly studied to explore the inner physical mechanism.[6-8] However, MD simulation is limited by the scale of the problem in time and dimension. Typically, the current computational facilities can only accomplish the simulation conditions of tens or hundreds of pico-seconds and hundreds of angstroms. Moreover, the small indenter size used in MD simulation (tens of angstroms) is often too small for practical applications. Thus, a different mathematical tool that can cover larger scales in time and dimension is required for the nano-scale simulation of indentation problems.

Another type of tool is a quasi-continuum method, which bridges atomistic simulations and continuum modeling. Several types of quasi-continuum methods have been developed in the research community.[9-14] The general ideas are similar to each other; that is, to use continuum assumptions to reduce the degrees–of–freedom and computational demands in

homogeneously and smoothly deformed regions, and to use the atomistic model to capture atomistic detail in regions where it is required. Some mechanical problems have been successfully solved by this method, but some issues are still under discussion, such as coupling between the continuous and atomistic regions, inertial and thermal effects.

Finite element analysis (FEA), based on continuum assumption and domain discretization, was developed to analyze micro-scale indentation and scratch problems. Dao et al.[15] and Bucaille et al.[16] used FEA to study instrumented sharp indentation and proposed analytical expressions of elastoplastic properties based on FEA results. Bucaille et al.[17] used FEA to perform scratch analysis using a cone-shape indenter in order to study the influence of the rheology. Most small-scale indentation experiments in reality are within sub-micron scale (hundreds of nanometers) due to the size of the indenter geometry. The feasibility and accuracy of FEA for this scale is being investigated.

Recent technological advances in indentation test facilities have led to the availability of accurate measurements of indentation force and indentation depth, from which hardness and other mechanical properties can be extracted. At the same time, theoretical studies have emerged to elucidate mechanical characterization and physical mechanisms.[1, 15, 17-21] For example, Goddard and Wilman[21] developed analytical models for friction coefficients of different indenters. Oliver and Pharr[19] and Doerner and Nix[20] developed methods to obtain hardness and the elastic modulus from the maximum load and the initial unloading slope. Recently, Dao et al.[15] and Bucaille et al.[16] constructed dimensionless functions to determine the plastic characterization of metals based on FEA simulation.

In practice, the success of FEA strongly depends on the accuracy in the material properties. For macro-scales, many standard experimental procedures have been developed to obtain these properties. In micro-scale, however, very limited experimental procedures are available due to scale-related issues.[15] First, it is difficult to fabricate a perfect indenter shape. The effect of inaccurate tip geometry becomes significant when the indentation depth is small. In addition, the measurement error in such a small scale can be critical. Sensitivity analysis with respect to experimental data provides important information in such a case.

The organization of the paper is as follows: In Section 2, the feasibility of FEA is first verified to be a useful and powerful tool to study micro-scale indentation by studying the indentation response of elastoplastic aluminum alloys. A new procedure using multivariable optimization is then proposed to identify the material properties of a gold film on a silicon substrate in Section 3. Since experimental error in such a small scale can significantly affect the accuracy of the identified material properties, sensitivity analysis of optimum material properties to experimental data is presented in Section 4, followed by conclusions in Section 5.

## 2. Indentation Simulation

As discussed above, finite element analysis is based on continuum assumption. When a problem reaches atomic scale, this assumption is no longer valid. The problems studied below are larger than atomic scale, but less than micrometers. The objective of this section is to verify the feasibility and accuracy of FEA at this scale. Since the motion of the indenter is slow and uniform, nonlinear static FEA is performed with elastoplastic material and contact constraints between the indenter and specimen. Since the deformation is large and non-uniform, the large deformation theory is used, by which detailed pile-up and sink-in effects can be more accurately captured. In this paper, a commercial program, ABAQUS[22], is used for numerical simulation.

### *2.1. Indentation Modeling*

The indentation by a diamond tip on two different types of aluminum alloys with a constant loading and unloading rates is implemented. The indented specimen has the dimensions of $300\,\mu\mathrm{m}$ depth and $300\,\mu\mathrm{m}$ length. The size of the sample must be large enough such that the effect of the far field boundary is not significant. In addition, the element near the indenter tip must be small enough so that the deformation at the tip can be captured accurately.

The Berkovich indenter is used in this model. The 3D Berkovich indenter is approximated by an axisymmetric 2D model. The projected area of the 2D cone is the same as that of the 3D Berkovich indenter. The equivalent half angle of the indenter becomes $\theta = 70.3^{\mathrm{O}}$.

The two aluminum alloys 6061 and 7075 are used as the indented specimen. A homogeneous section property is assumed in the model. Table 1 shows the material properties for the two aluminum alloys. In Table 1, *E* is the elastic modulus, $\sigma_Y$ the initial yield stress, *n* the strain hardening exponent, and $\nu$ Poisson's ratio. The indenter is made of diamond with a high elastic modulus of 1,100 GPa.

**Table 1**. Material properties of aluminum alloys

| Material | $E(\mathrm{GPa})$ | $\sigma_Y(\mathrm{MPa})$ | $n$ | $\nu$ |
|---|---|---|---|---|
| Al 6061 | 66.8 | 284 | 0.08 | 0.33 |
| Al 7075 | 70.1 | 500 | 0.122 | 0.33 |

The total strain is decomposed by two parts, the elastic strain $\varepsilon_e$ and the plastic strain $\varepsilon_p$, such that

$$\varepsilon = \varepsilon_e + \varepsilon_p . \tag{1}$$

The elastic behavior is modeled by the elastic modulus and the plastic behavior is modeled by a simple power law,

$$\sigma = \begin{cases} E\varepsilon & \sigma \le \sigma_y \\ K\varepsilon^n & \sigma > \sigma_y \end{cases}, \tag{2}$$

where $K$ is a strength coefficient. Considering continuity at the initial yield point,

$$\sigma_Y = E\varepsilon = K\varepsilon^n, \quad (3)$$

such that $K = E^n \sigma_Y^{1-n}$. The material behaviors of AL 6061 and AL 7075 are shown in Figure 1.

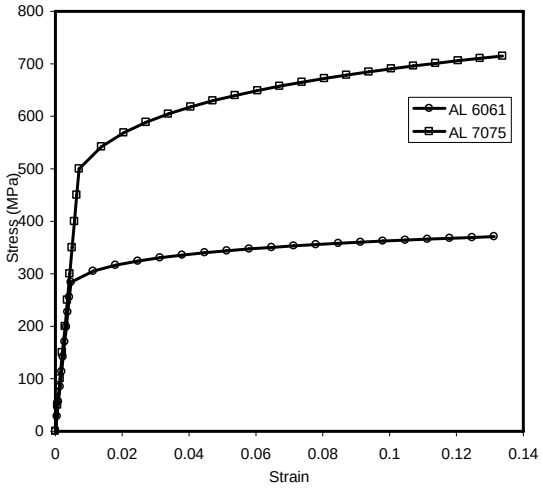


**Figure 1**: Elastoplastic material behaviors of aluminum alloys

An axi-symmetric finite element model is constructed to analyze the indentation process (Figure 2). Linear quadrilateral elements are used to build the indented specimen. Due to the high elastic modulus and brittle behavior, the diamond indenter is modeled using a rigid body. A total of 4,763 elements are used to model the specimen. In order to represent indentation accurately, the elements near the indenter have a small size with an edge length of $1.5\,\mu\text{m}$. Far from the contact area, the elements have a typical edge length of $12\,\mu\text{m}$.

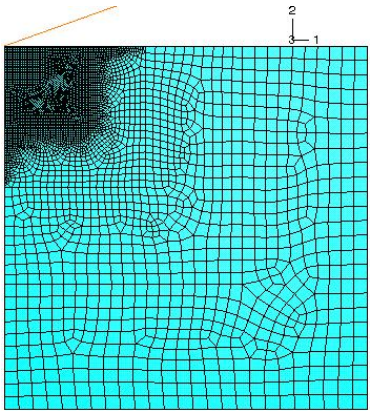


**Figure 2**: Finite element model of axi-symmetric indentation with a conical tip

The surface-to-surface contact constraint is established between the rigid indenter and top surface of the specimen. The impenetrability condition is imposed between the "master surface" indenter and the "slave surface" specimen. Mathematically, the contact problem is equivalent to constrained optimization, which can be solved using the Lagrange multiplier method. Since the friction coefficient is difficult to calculate and since the indentation problem does not have large slip, frictionless contact is assumed. However, friction will be an important factor in the scratch simulation.

In Figure 2, the bottom surface of the specimen is fixed in the $y$-direction and the left side is fixed in the $x$-direction. The incremental solution procedure is displacement-controlled with a loading/unloading rate of $20\,\mu\text{m/sec}$ in the $y$-direction. For AL 7075, the indentation is performed for 0.75 seconds and then the indenter is removed in order to observe the elastic spring-back and the plastic permanent deformation. For the AL 6061, the indentation is carried out for 0.5 seconds. Even though the indentation depth is only $15\,\mu\text{m}$, the contact constraints bring nonlinearity.

### *2.2 Simulation and Experimental Results*

The indentation force as a function of the indentation depth during loading and unloading steps is an important factor in evaluating the elastoplastic properties of the material. Figure 3 shows the relation between the indentation force and the indentation depth of both aluminum alloys. For AL 7075, the maximum force reaches around 10 N when the indentation depth is $15\,\mu\text{m}$. For AL 6061, the maximum force reaches around 3 N when the indentation depth is $10\,\mu\text{m}$. The slope of the force-depth curve gradually increases because the material has strain hardening and the contact area is increased. The analysis results show a consistent behavior with the experiments[15], which verifies the feasibility and accuracy of FEA for small scale indentation problems.

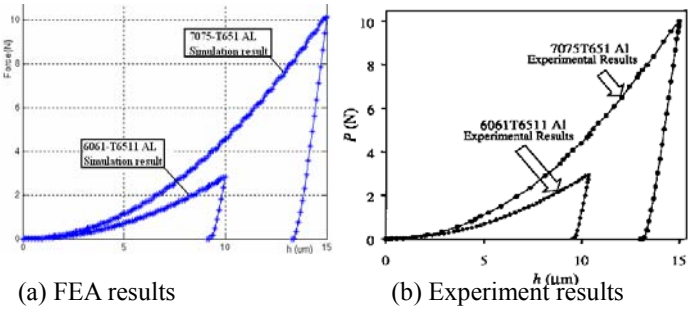


(a) FEA results (b) Experiment results

**Figure 3**: Indentation response of aluminum alloys by finite element analysis and experiment[15]

The equivalent stress distribution of AL 7075 after unloading is shown in Figure 4. As expected, the maximum residual stress occurs at the tip location. In addition, the residual stress at the pile-up region is also high. The equivalent plastic strain in Figure 5 indicates that the majority of the volume under the indenter has plastic strains exceeding 19.41%, and the maximum strain is 233%.

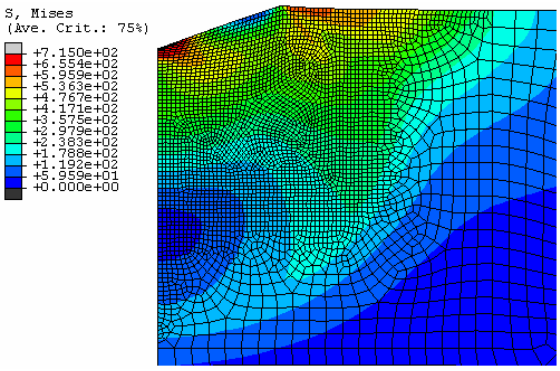


**Figure 4**: Equivalent stress contour plot for AL 7075 after unloading (unit: MPa)

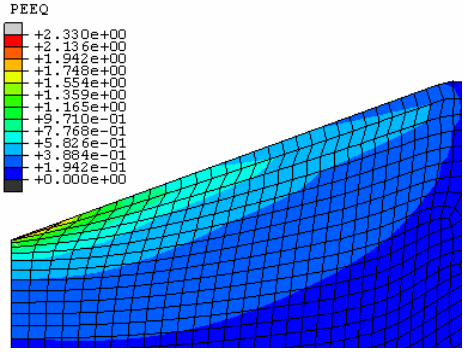


**Figure 5**: Effective plastic strain near the indenter tip

## 3. Identification of the Material Properties of a Gold Film

Based on the study of aluminum alloys, the material properties of a gold film on a silicon substrate are estimated by comparing the history of the force-depth curve between the indentation experiment and FEA. The 180 nm thick crystalline gold used in the film is produced by the electron beam evaporation process. The gold material has 99.99% purity with no native oxide. Since the grain size of the gold is much smaller than that of the bulk material, the material properties are expected to be different from those of bulk materials. The crystalline gold is modeled using an elastoplastic material with strain hardening. The silicon substrate is assumed to be elastic because the experiment shows no permanent deformation.

In Section 2, the geometry of the indenter is assumed to be a conical shape. The radius of the tip is ignored because it is relatively small, compared to the indentation depth. However, when the indentation depth is small, the detailed geometry of the indenter can affect the results from both experiment and analysis. For example, the indentation depth of the gold film is around 50 nm, whereas the radius of the tip is around 1,000 nm. Since only a small portion of the tip is indented, the tip can be considered a sphere. Then the accuracy of the indenter geometry contributes to the force-depth response during the indentation.

In general, the indenter geometry can be obtained from the Scanning Electron Microscopy image (Figure 6). However, the tip geometry contains a certain level of uncertainty because it is obtained from pixel images. The effect of such uncertainty is usually small when the indentation depth is large enough. However, the effect becomes significant when the indentation depth is less than 100 nm, which is the case of interest. By fitting scanned points in the image, it is shown in Figure 6 that the radius of the tip is between $1.05\,\mu\mathrm{m}$ and $1.2\,\mu\mathrm{m}$. Due to the approximation of the fitting, it is not accurate to use the fitted curve as the indenter shape in the study. The unique feature of the paper is the inclusion of the tip geometry as a design variable during material property identification.

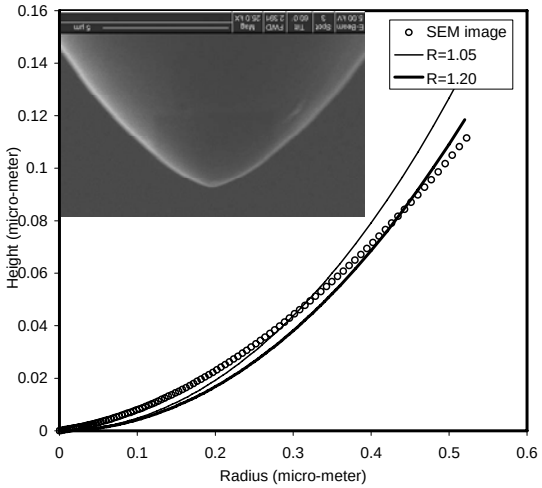


**Figure 6**: The tip geometry of the indenter from SEM and its approximations with a sphere.

A constrained nonlinear multivariable optimization method is implemented to identify the material properties as well as the radius of the tip. This method seeks the minimum of a function (the error between the experiment and numerical analysis) of several variables starting with the initial estimation. The design variables are the elastic modulus $E$, initial yield stress $\sigma_Y$, strain hardening exponent $n$, Poisson's ratio $\nu$, and the indenter radius $r$.

The objective function is the error in the force-depth curves between the experiment and FEA. Figure 7 shows the force-depth curve from the experiment and the simulation with the initially estimated material properties (Table 2). Let the indentation depth is discretized by $N$ discrete points, out of which the loading step has $N_1$ data points, while the unloading step has $N_2$ points. Mathematically, the objective function can then be defined as

$$f = \frac{1}{N}\sum_{i=1}^{N}(F_s^i - F_t^i)^2\,, \tag{4}$$

where $F_s^i$ and $F_t^i$ are indentation forces from experiment and analysis, respectively, at the *i*-th indentation depth. In Figure 7, the indentation depth of the unloading step is reversed such that the indentation depth continuously increases during the unloading step.

**Table 2**. Initial and identified material properties

| Design variable | Lower bound | Upper bound | Initial estimation | Optimized value |
|---|---|---|---|---|
| $E$(GPa) | 25 | 80 | 78.5 | **33.35** |
| $\sigma_Y$(MPa) | 150 | 450 | 300 | **353.71** |
| $n$ | 0.05 | 0.3 | 0.122 | **0.115** |
| $\nu$ | 0.1 | 0.45 | 0.3 | **0.220** |
| $r$(μm) | 1.05 | 1.2 | 1.1 | **1.090** |

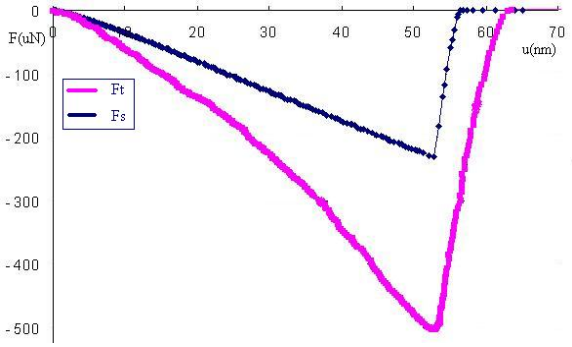


**Figure 7**: Indentation force vs. indentation depth with initial estimation of material properties

In order to compute the difference between the simulation force $F_s^i$ and experimental force $F_t^i$, the two forces should be calculated at the same indentation depth $u_i$. However, it is impractical to obtain the same simulation data pair $(F_s^i, u_i)$ with the experiment data pair $(F_t^i, u_i)$ because both are performed independently. In order to make this comparison consistent, the experimental data are approximated using a polynomial response. The approximate response has the following expression:

$$F_t(u) = \sum_{i=1}^{k} \beta_i x_i(u), \tag{5}$$

where $F_t(u)$ is the approximated indentation force, $\beta_i$ the regression coefficient, and $x_i(u)$ the regression basis. In this paper, a monomial basis of order five is used; i.e., $k = 6$ and $[x_j(u)] = [1 \quad u \quad u^2 \quad u^3 \quad u^4 \quad u^5]$. Since the force-depth curves for loading and unloading are different, two responses are constructed: one for the loading step and the other for the unloading step. Figure 8 shows the experimental data points and the response surface constructed by calculating the regression coefficients in Eq. (5), for both the loading and unloading steps. In Figure 8(b), the abscissa in the unloading step represents the tip location relative to the maximum depth from the loading step.

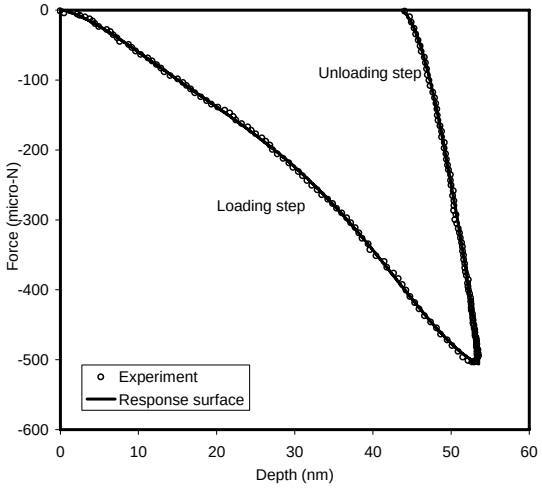


**Figure 8**: Force distribution in the loading and unloading steps

Once the response surfaces $F_t(u)$ of the experimental data have been obtained, the optimization problem can be solved to minimize the error function in Eq. (4). The optimized material properties and the radius of the tip are shown in the last column of Table 2. The most significant difference between initial and optimum values occurs in the elastic modulus.

Figure 9 shows the force-depth comparison between the experiment data, initial and optimum designs. The maximum indentation force at optimization is -495.69 $\mu N$, while that from experiment is -495.04 $\mu N$. The error in the objective function reduces significantly from the initial design (14887.1) to the final optimization (116.7). The force-depth curve with optimization values matches the experiment curve much better than the initial design parameters, which also shows the accuracy of the optimization. Since the slope of the unloading curve is strongly related to the elastic modulus, the difference in the unloading slope between the initial and the final designs verifies that the initial estimation of the elastic modulus was too high.

In the micro-scale indentation, indenter geometry plays an important role in the results. Figure 10 compares the results of identification with and without inclusion of the radius of the tip as a parameter. It is clear that the identified material properties with the radius of the tip fit well with the experimental results.

## 4. Sensitivity Analysis

Indentation forces and depths that are measured from the experiment are used as a reference during the material property identification. These experimental data are fitted using response surfaces such that continuous responses can be obtained. The identification problem then minimizes the difference between these response surfaces and the results from FEA by changing the material properties and the tip radius. Since experimental

data may have measurement errors and noise, they are not accurate in general and their effect on the identified parameter values can be significant. This is especially so because, since the magnitudes of forces and depths are small in the thin film indentation, these errors and noises may significantly affect the accuracy of the identified material properties. The effect of identified parameter values with respect to the experimental data can be found using the sensitivity analysis technique.[23]

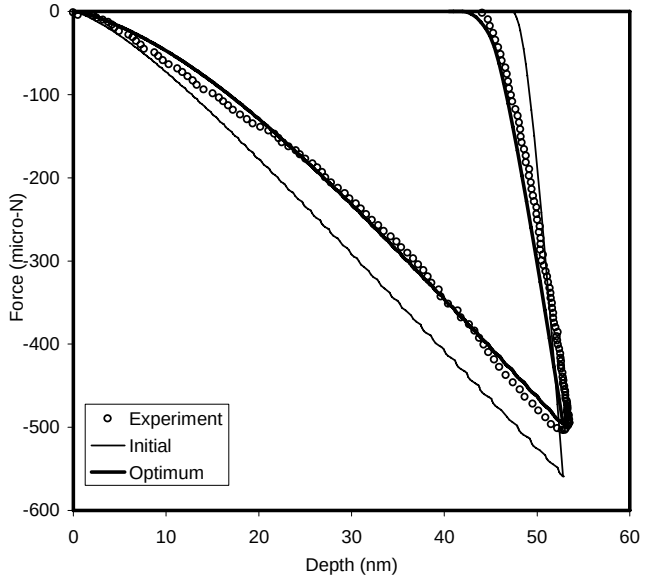


**Figure 9**: Force and depth comparisons of experimental, initial design and optimized results

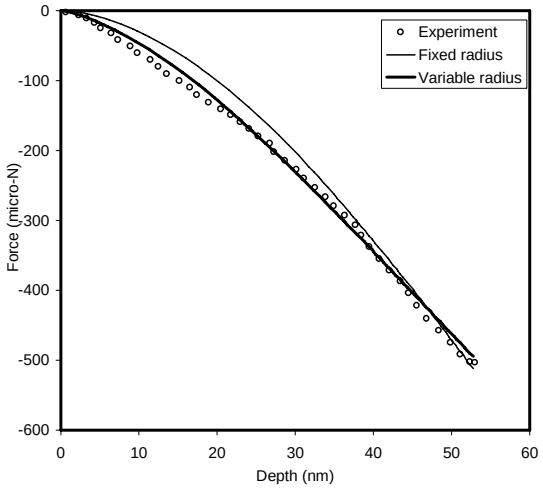


**Figure 10**: Comparison of the force-displacement curve with the identified material properties (with and without tip radius)

In practice, calculating sensitivity with respect to much experimental data is exhaustive and cannot provide physically meaningful results. Since experimental data are represented by the coefficients of the response surface, the sensitivities with respect to these coefficients are calculated in this paper. The sensitivity information will provide the dependence of the identified material parameters on the accuracy of experimental data.

### *4.1. Significance of Coefficients*

Before performing sensitivity analysis, the test that can determine the significance of each approximation coefficient in Eq. (5) is conducted. Such a test is useful in determining the importance of each regression variable in the model. For example, the model can be more effective by including additional variables. On the other hand, no significant difference can be found by deleting one or more variables that are already in the model.[24]

Let us consider the regression basis $x_j$ and its coefficient $\beta_j$. It is clear that if the coefficient $\beta_j$ is small, then $x_j$ can be deleted from the model without significantly affecting the results. More specifically, the criterion of the deletion is based on the following test statistic:

$$t_{\beta_j} = \frac{\beta_j}{\sqrt{\sigma^2 C_{jj}}}, \tag{6}$$

where $C_{jj}$ is the diagonal element of $(\mathbf{X}^T\mathbf{X})^{-1}$ corresponding to $\beta_j$, $\sigma^2$ is the estimated variance given by

$$\sigma^2 = \frac{SS_E}{N-k}, \tag{7}$$

and $\mathbf{X}$ is the regression variable matrix, defined as

$$[\mathbf{X}] = \begin{bmatrix} x_1^1 & x_2^1 & \dots & x_k^1 \\ x_1^2 & x_2^2 & \dots & x_k^2 \\ \vdots & \vdots & \ddots & \vdots \\ x_1^N & x_2^N & \dots & x_k^N \end{bmatrix}, \tag{8}$$

where $k$ is the number of the regression bases and $N$ is the number of experiment observations. In Eq. (7), $SS_E$ is the square-sum residuals, defined as

$$SS_E = \sum_{i=1}^{N} \left( F_t^i - \bar{F}_t^i \right)^2, \tag{9}$$

where $F_t^i$ is the observation value from the experiment and $\bar{F}_t^i$ the fitted value.

The test statistic is distributed as the student distribution $t_{N-k}$.[24] If the test statistic is small, then the contribution of the regression variable and its coefficient is small. In general, a critical statistic $t_{\alpha/2,N-k}$, depending on parameter $\alpha$, is first determined. The regression basis $x_j$ and its coefficient $\beta_j$ are kept if its test statistic is larger than the critical statistic, as

$$\left| t_{\beta_j} \right| > t_{\alpha/2,N-k}, \tag{10}$$

which means that the effect of the regression basis is significant.[24] In the identification problem of Section 3, the rejection criterion in the student's distribution is selected as $\alpha = 0.05$. Thus, the critical statistic for both loading and unloading steps becomes 1.960.

In the nonlinear regression in the loading and unloading steps, the test statistics for each regression coefficient is shown in Table 3. It is noted that for the loading step the magnitudes of test statistics are increased at the higher order of polynomials. The opposite trend is observed for the unloading step. All test statistics are greater than the critical statistic except for $\beta_0$ in the loading step. Thus, the constant term in the response surface of the loading step can be removed without significantly affecting the result.

**Table 3.** Nonlinear regression and significance statistics

| Coef. | Loading step | | Unloading step | |
|---|---|---|---|---|
| | Value | Stat. | Value | Stat. |
| $\beta_0$ | 6.945e−1 | 0.649 | 4.966e+2 | −279.179 |
| $\beta_1$ | −2.391e+0 | −6.263 | 8.476e+1 | 23.009 |
| $\beta_2$ | −6.304e−1 | −14.829 | −6.953e+0 | −3.335 |
| $\beta_3$ | 3.358e−2 | 17.101 | 1.235e+0 | 2.684 |
| $\beta_4$ | −8.060e−4 | −20.324 | −1.353e−1 | −3.156 |
| $\beta_5$ | 6.585e−6 | 22.728 | 4.638e−3 | 3.295 |

### *4.2. Sensitivity Analysis*

With the regression variables that have significant effects on the response, the sensitivities of the identified parameters with respect to the regression coefficients are calculated. Consider the general form of an optimization problem with inequality constraints, defined as

$$\begin{aligned} &\text{minimize} && f(\mathbf{d}, p) \\ &\text{subject to} && g_j(\mathbf{d}, p) \geq 0, \quad j = 1,\ldots,k \end{aligned}, \tag{11}$$

where $\mathbf{d} = [E, \sigma_Y, n, \nu, r]$ is the vector of material properties and indenter geometry that can be changed during the optimization, and $p$ is a fixed parameter during the optimization (for example, a regression coefficient). The goal is to calculate the sensitivities of the optimized parameter $\mathbf{d}^*$ with respect to the regression coefficient $p = \beta_i$.

The optimality condition for the above optimization problem can be stated using the Karush-Kuhn-Tucker condition,[23] as

$$\begin{aligned} &\frac{\partial f}{\partial d_i} - \sum_{j=1}^{r} \frac{\partial g_j}{\partial d_i}\lambda_j = 0, && i = 1,\ldots,m \\ &g_j = 0, && j = 1,\ldots,q \end{aligned}, \tag{12}$$

where $m$ is the number of identified parameters, $q$ the number of active constraints when the optimization problem is converged, and $\lambda_j$ the Lagrange multiplier for the *j*-th active constraint. Since the optimality condition must satisfy for all parameters, Eq. (12) can be differentiated with respect to parameter $p$ to obtain[23]

$$\begin{aligned} &[\mathbf{A} - \mathbf{Z}]\frac{\partial \mathbf{x}^*}{\partial p} - [\mathbf{M}]\frac{\partial \boldsymbol{\lambda}}{\partial p} + \frac{\partial(\nabla f)}{\partial p} - \frac{\partial[\mathbf{M}]}{\partial p}\boldsymbol{\lambda} = 0 \\ &[\mathbf{M}]^T \frac{\partial \mathbf{d}^*}{\partial p} + \frac{\partial \mathbf{g}}{\partial p} = 0 \end{aligned}, \tag{13}$$

where $\boldsymbol{\lambda}$ is the vector of Lagrange multipliers obtained while solving the optimization problem, $(\nabla f)_j = \partial f / \partial d_j$ is the derivative of the objective function, $[\mathbf{M}] = [\partial g_j / \partial d_i]$ is the derivative of the active constraints, $[\mathbf{A}]$ is the Hessian matrix of the objective function, $[\mathbf{Z}]$ is the matrix defined as

$$[Z_{kl}] = \sum_{j=1}^{q} \frac{\partial^2 g_j}{\partial d_k \partial d_l}\lambda_j \,. \tag{14}$$

The sensitivity equation (13) is a linear system of equations and solves for $\partial \mathbf{d}^* / \partial p$ and $\partial \boldsymbol{\lambda} / \partial p$.

When there is no active constraint, the sensitivity formulas in Eq. (13) can significantly be simplified, as

$$[\mathbf{A}]\frac{\partial \mathbf{d}^*}{\partial p} + \frac{\partial(\nabla f)}{\partial p} = 0 \,. \tag{15}$$

Thus, in order to calculate the sensitivity of the identified parameters with respect to a regression coefficient, the gradient of objective function and its Hessian matrix are required.

From the expression of the objective function in Eq. (4), these terms can be calculated as

$$\frac{\partial f}{\partial d_j} = \frac{1}{N}\sum_{i=1}^{N} 2(F_s^i - F_t^i)\frac{\partial F_s^i}{\partial d_j} \tag{16}$$

and

$$\frac{\partial^2 f}{\partial d_j \partial d_k} = \frac{2}{N}\sum_{i=1}^{N}\left(\frac{\partial F_s^i}{\partial d_j}\frac{\partial F_s^i}{\partial d_k} + (F_s^i - F_t^i)\frac{\partial^2 F_s^i}{\partial d_j \partial d_k}\right). \tag{17}$$

In addition, the coupled term can be expressed by

$$\frac{\partial}{\partial p}\left(\frac{\partial f}{\partial d_j}\right) = -\frac{2}{N}\sum_{i=1}^{N}\frac{\partial F_t^i}{\partial p}\frac{\partial F_s^i}{\partial d_j}. \tag{18}$$

In the case of the loading step,

$$\frac{\partial}{\partial \beta_m}\left(\frac{\partial f}{\partial d_j}\right) = -\frac{2}{N}\sum_{i=1}^{N_1}(u_i)^{m-1}\frac{\partial F_s^i}{\partial d_j}. \tag{19}$$

Or, in the case of the unloading step,

$$\frac{\partial}{\partial \beta_m}\left(\frac{\partial f}{\partial d_j}\right) = -\frac{2}{N}\sum_{i=1}^{N_2}(u_i)^{m-1}\frac{\partial F_s^i}{\partial d_j}, \tag{20}$$

where $N_1 = 431$ and $N_2 = 26$ are taken from the loading and unloading steps, respectively.

In order to solve the sensitivity equation (15), the derivatives are calculated using the central finite difference method. For example, the derivative of $F_s^i$ can be approximated by

**Table 4**. Normalized sensitivity of identified parameters with respect to regression coefficients (loading step)

| Sensitivity | $\beta_2$ | $\beta_3$ | $\beta_4$ | $\beta_5$ | $\beta_6$ |
|---|---|---|---|---|---|
| $(\partial E^* / \partial \beta_i) / E^*$ | −3.0169E−1 | −1.5676E+1 | 8.3976E+2 | −4.3792E+4 | −2.2389E+6 |
| $(\partial \sigma_Y^* / \partial \beta_i) / \sigma_Y^*$ | −2.4836E−1 | 1.0788E+1 | 9.6310E+2 | 5.7078E+4 | 3.0602E+6 |
| $(\partial n^* / \partial \beta_i) / n^*$ | 5.6896E−1 | −3.9924E+1 | −3.2153E+3 | −1.8563E+5 | −9.8310E+6 |
| $(\partial \nu^* / \partial \beta_i) / \nu^*$ | 1.3138E−1 | 2.2072E+1 | 1.6496E+3 | 9.9280E+4 | 5.4791E+6 |
| $(\partial r^* / \partial \beta_i) / r^*$ | 2.0355E−2 | −3.1191E+0 | −2.4801E+2 | −1.4552E+4 | −7.9281E+5 |

**Table 5**. Normalized sensitivity of identified parameters with respect to regression coefficients (unloading step)

| Sensitivity | $\beta_1$ | $\beta_2$ | $\beta_3$ | $\beta_4$ | $\beta_5$ | $\beta_6$ |
|---|---|---|---|---|---|---|
| $(\partial E^* / \partial \beta_i) / E^*$ | 4.8389E−3 | 1.4638E−2 | −8.3065E−3 | −7.6433E−1 | −1.0663E+1 | −1.1914E+2 |
| $(\partial \sigma_Y^* / \partial \beta_i) / \sigma_Y^*$ | −1.0818E−2 | −8.7777E−2 | −7.1156E−1 | −5.9490E+0 | −5.1035E+1 | −4.4716E+2 |
| $(\partial n^* / \partial \beta_i) / n^*$ | 3.0652E−2 | 2.7196E−1 | 2.2545E+0 | 1.9044E+1 | 1.6432E+2 | 1.4449E+3 |
| $(\partial \nu^* / \partial \beta_i) / \nu^*$ | 2.1091E−3 | 6.6835E−2 | 7.9877E−1 | 8.0913E+0 | 7.7826E+1 | 7.3512E+2 |
| $(\partial r^* / \partial \beta_i) / r^*$ | −1.9912E−4 | −4.5010E−3 | −4.2827E−2 | −3.8398E−1 | −3.4298E+1 | −3.0889E+1 |

$$\frac{\partial F_s^i}{\partial d_j} = \frac{F_s^i(d_j + \Delta d_j) - F_s^i(d_j - \Delta d_j)}{2\Delta d_j}, \tag{21}$$

where $\Delta d_j$ is a small perturbation of the parameters. The second-order derivatives of $F_s^i$ are much smaller than the first term and, thus, they are negligible.

Tables 4 and 5, respectively, show the sensitivities of the identified parameters with respect to the regression coefficients at the loading and unloading steps. Since the magnitudes of the parameters are different, the sensitivities are normalized using their identified values.

As shown in the two tables, the sensitivity of the identified parameters increases at the higher order polynomials for both loading and unloading steps. This result foresees the difficulty in the identification problem. In the view of the regression coefficients in Table 3, the values of the coefficients are smaller at the higher order polynomials, but they are more sensitive to the identified parameters.

In both the loading and unloading steps, the hardening exponent always has the biggest sensitive value compared with other variables with respect to each regression coefficient, which means that the hardening exponent is the most sensitive variable due to the error in the experiment measurement.

## 5. Conclusions

Mechanical properties of materials in micro-scales are different from those of bulk materials. In this paper, a new procedure is proposed to identify the material properties of elastoplastic thin gold films by (i) including the tip geometry of the indenter as a design variable, (ii) approximating the experimental data using polynomial responses, and (iii) performing sensitivity analysis with respect to regression coefficients.

A comparison between experiment and analysis is made for the responses throughout the whole indentation process, not the data at the end of the process. This is important, because the material shows loading history dependent responses. The uncertainty related to the indenter tip geometry is taken care of by including the radius of the tip as a variable of the optimization. Two fifth-order response surfaces are constructed to fit the experimental data and a test statistic is used to identify unessential coefficients. It turns out that the constant term of the load step is unessential and, thus, removed. The response surfaces have smaller values of coefficients at the higher-order terms, which is common for the regular response surfaces. However, the test statistics show different trends for loading and unloading steps. In the case of the loading step, the test statistic is higher for the higher-order terms. In the case of unloading step, however, it is higher for the lower-order terms. Sensitivity with respect to the regression coefficients shows consistent trends: higher-order terms have higher sensitivities. This trend foresees difficulties in material property identification, as smaller coefficients have higher sensitivity. It turns out that the hardening exponent is the most sensitive variable due to the error in the experiment measurement.

## References


1. Stauss, S., et al., *Determining the stress-strain behaviour of small devices by nanoindentation in combination with inverse methods.* Microelectronic Engineering, 2003(67-68): p. 818-825.
2. Bertrand-Lambotte, P., et al., *Understanding of automotive clearcoats scratch resistance.* Thin Solid Films, 2002(420 - 421): p. 281-286.
3. Kim, D.H., J.K. Kim, and P. Hwang, *Anisotropic tribological properties of the coating on a magnetic recording disk.* Thin Solid Films, 2000(360): p. 187-194.
4. Hodzic, A., et al., *Application of nano-indentation, nano-scratch and single fibre tests in investigation of interphases in composite materials.* Micron, 2001(32): p. 765-775.

5. Landman, U., et al., *Atomistic Mechanisms and Dynamics of Adhesion, Nanoindentation, and Fracture.* Science, 1990. **248**(4954): p. 454-461.
6. Liang, H., et al., *Crystalline Plasticity on Copper (001), (110), and (111) Surfaces during Nanoindentation.* CMES, 2004. **6**(1): p. 105-114.
7. Komanduri, R., N. Chandrasekaran, and L.M. Raff, *MD simulation of indentation and scratching of single crystal aluminum.* Wear, 2000(240): p. 113-143.
8. Mulliah, D., et al., *Molecular dynamic simulations of nanoscratching of silver (100).* Nanotechnology, 2004(15): p. 243-249.
9. Tadmor, E.B., M. Ortiz, and R. Phillips, *Quasicontinuum analysis of defects in solids.* Philosophical Magazine A, 1996. **73**(6): p. 1529-1563.
10. Miller, R.E. and E.B. Tadmor, *The quasicontinuum method: Overview, applications and current directions.* Journal of Computer-Aided Materials Design, 2002(9): p. 203-239.
11. Mortensen, J.J., J. Schiotz, and K.W. Jacobsen, *The quasicontinuum method revisited.* Challenges in Molecular Simulations, 2002. **4**(119): p. 119-136.
12. Shenoy, V.B., et al., *Quasicontinuum Models of Interfacial Structure and Deformation.* Physical Review Letters, 1998. **80**(4): p. 742-745.
13. Zhu, T., et al., *Predictive modeling of nanoindentation-induced homogeneous dislocation nucleation in copper.* Journal of the Mechanics and Physics of Solids, 2004(52): p. 691 -724.
14. Zhang, P., et al., *An atomistic-based continuum theory for carbon nanotubes: analysis of fracture nucleation.* J. of the Mechanics and Physics of Solids, 2004. **52**: p. 977-998.
15. Dao, M., et al., *Computational Modeling of the Forward and Reverse Problems in Instrumented Sharp Indentation.* Acta materialia, 2001(49): p. 3899-3918.
16. Bucaille, J.L., et al., *Determination of plastic properties of metals by instrumented indentation using different sharp indenters.* Acta Materialia, 2003. **51**: p. 1663-1678.
17. Bucaille, J.L., E. Felder, and G. Hochstetter, *Mechanical analysis of the scratch test on elastic and perfectly plastic materials with the three-dimensional finite element modeling.* Wear, 2001(249): p. 422-432.
18. Larsson, P.L., et al., *Analysis of Berkovich Indentation.* Int. J. Solids Structures, 1996. **33**(2): p. 221-248.
19. Oliver, W. and G. Pharr, *An improved technique for determining hardness and elastic modulus using load and displacement sensing indentation experiments.* J Mater Res, 1992. **7**(6): p. 1564-1583.
20. Doener, M.F. and W.D. Nix, *A Method for Interpreting the Data From Depth-Sensing Indentation Instruments.* J. Mater. Res., 1986. **1**: p. 601.
21. Goddard, J. and H. Wilman, *A theory of friction and wear during the abrasion of metals.* Wear, 1962. **5**: p. 114-135.
22. AbaqusInc., *Abaqus User's Manual.* Rising Sun Mills, 166 Valley St. Providence, RI, 2005.
23. Haftka, R.T. and Z. Gurdal, *Elements of Structural Optimization*. 3rd ed, ed. G.M.L. Gladwell. 1992, Dordrecht/Boston/London: Kluwer Academic Publishers.
24. Myers, R.H. and D.C. Montgomery, *Response Surface Methodology*. 1995, New York: John Wiley & Sons, Inc.